

Low-field Onset of Wannier-Stark Localization in a Polycrystalline Hybrid Organic Inorganic Perovskite

Daniel Berghoff

Paderborn University

Johannes Bühler

University of Konstanz

Mischa Bonn

Max Planck Institute for Polymer Research

Alfred Leitenstorfer

University of Konstanz

Torsten Meier

University of Paderborn <https://orcid.org/0000-0001-8864-2072>

Heejae Kim (✉ kim@mpip-mainz.mpg.de)

Max Planck Institute for Polymer Research

Article

Keywords: Wannier-Stark localization, Electron confinement, Ultrafast Biasing, Optical modulation, Hybrid perovskites

Posted Date: April 8th, 2021

DOI: <https://doi.org/10.21203/rs.3.rs-386040/v1>

License:   This work is licensed under a Creative Commons Attribution 4.0 International License.

[Read Full License](#)

Version of Record: A version of this preprint was published at Nature Communications on September 29th, 2021. See the published version at <https://doi.org/10.1038/s41467-021-26021-4>.

Low-field Onset of Wannier-Stark Localization in a Polycrystalline Hybrid Organic Inorganic Perovskite

*Daniel Berghoff^{†1}, Johannes Bühler^{‡2}, Mischa Bonn³, Alfred Leitenstorfer², Torsten Meier^{*1}, Heejae Kim^{*3}*

¹Department of Physics, Paderborn University, D-33098 Paderborn, Germany

²Department of Physics and Center for Applied Photonics, University of Konstanz, D-78457 Konstanz, Germany

³Department of Molecular Spectroscopy, Max Planck Institute for Polymer Research, D-55128 Mainz, Germany

KEYWORDS

Wannier-Stark localization, Electron confinement, Ultrafast Biasing, Optical modulation, Hybrid perovskites

ABSTRACT

Control over light propagation in a material by applying external fields is at the heart of photonic applications. Here, we demonstrate ultrafast modulation of the optical properties in the room temperature polycrystalline MAPbI₃ perovskite using phase-stable terahertz pulses, centered at 20 THz. The biasing field from the THz pulse creates extreme localization of electronic states in the *ab* plane – Wannier-Stark localization. This quasi-instantaneous reduction of dimensionality (from 3D to 2D) causes a marked change in the absorption shape, enabling the modulation depth to be tens of percent at moderate field strengths (3 MV/cm). The notably low-field onset results from a narrow electronic bandwidth, a large relevant lattice constant, and the coincidence of the two along the same direction in this tetragonal perovskite. We show that the transient optical response is in fact dominated by the least dispersive direction of the electronic band structure, facilitating a substantial modulation despite the arbitrary arrangement of the individual crystallites. The demonstration of THz-field-induced optical modulation in a solution-processed, disordered, and polycrystalline material is of substantial potential significance for novel photonic applications.

Introduction

The intriguing properties of electrons in periodic potentials in the presence of strong external electric fields are highly relevant for photonic applications, including optical modulators, optical switches, and optical signal processing. Drastic changes in optical properties can be achieved via localization of electronic states using externally applied fields. In the presence of strong external electric fields E , the continuum of electronic energy bands splits into a series of discrete levels in the direction of the field¹, and the corresponding wave functions are confined on a length scale given by $\Delta/(eE)$, where Δ is the energetic width of the electronic band in the absence of biasing.

These localized states, the Wannier-Stark states^{2,3}, are equally spaced both in energy by an amount eED , and in space by the lattice period D . Since a spatial separation of nD lattice periods results in an energy shift of $neED$ with respect to the central spatially-direct ($n = 0$) transition, this Wannier-Stark localization leads to strong spectral modulation of the interband absorption continuum below and above the optical band gap.

The quantum confinement induced by external fields is an extreme state of matter and has never been achieved under static biasing in natural solids but only in artificial superlattices⁴⁻⁸. So far, only one natural solid, a single crystal GaAs⁸ has allowed for achieving the Wannier-Stark localization transiently by virtue of the recent availability of extremely intense and phase-stable pulses of multi-terahertz radiation^{9,10}. The ultrafast biasing fields could reach amplitudes up to several tens of MV/cm^{9,10}, i.e., field strengths comparable to the interatomic fields. For GaAs, an optimally oriented single crystal was required to observe Wannier-Stark localization with the required field strengths exceeding 10 MV/cm⁸.

Here, we demonstrate the transient Wannier-Stark localization at a substantially lower field strength in a disordered, solution-processed, polycrystalline film of methylammonium lead iodide perovskite (MAPbI₃, Fig. 1(a)). Already at relatively modest field strengths, the thin film's optical transmission is modified by tens of percent. To resolve optical transitions to individual Wannier-Stark states in, e.g., absorption spectra, their energetic spacing needs to be larger than the (total) linewidth Γ , i.e., $eED > \Gamma$ ^{4,5,11}. Due to the small lattice constant of bulk crystals and the large linewidth which results from the scattering of electrons with lattice vibrations and other electrons, the requirement $eED > \Gamma$ can typically not be fulfilled under stationary external fields below the strength where the dielectric breakdown occurs^{6,7}. At room temperature, however, this material exhibits a tetragonal structure with lattice parameters of $a = 8.8 \text{ \AA}$ and $c = 12.5 \text{ \AA}$ by the expansion

of the cubic perovskite unit cell^{12,13}. The periodicities are nearly twice as large as the lattice parameter $a = 5.6 \text{ \AA}$ of cubic GaAs⁸.

We will show that the large relevant lattice constant (Fig. 1(a)), the small width of electronic energy bands (Fig. 1(b)), and the coincidence of these two along the same high-symmetry direction lead to Stark localization in this organic perovskite at field amplitudes as low as 3 MV/cm, i.e., at a fraction of the field strength required to enter this regime in optimally oriented, single-crystalline GaAs. Moreover, the measured differential spectra containing the overall effects from arbitrarily oriented microcrystals are qualitatively well-described by a two-band model with a cosine band structure. By considering different orientations of the microcrystals in our simulations, we demonstrate that the contribution from the direction with the largest periodicity, i.e., the $\overline{\Gamma Z}$ direction $c = 12.5 \text{ \AA}$, strongly dominates the transient changes of the optical response. These findings, together with its renowned characteristics, make MAPbI₃ a strong candidate for cost-effective, efficient, fast, and sensitive optical modulator materials.

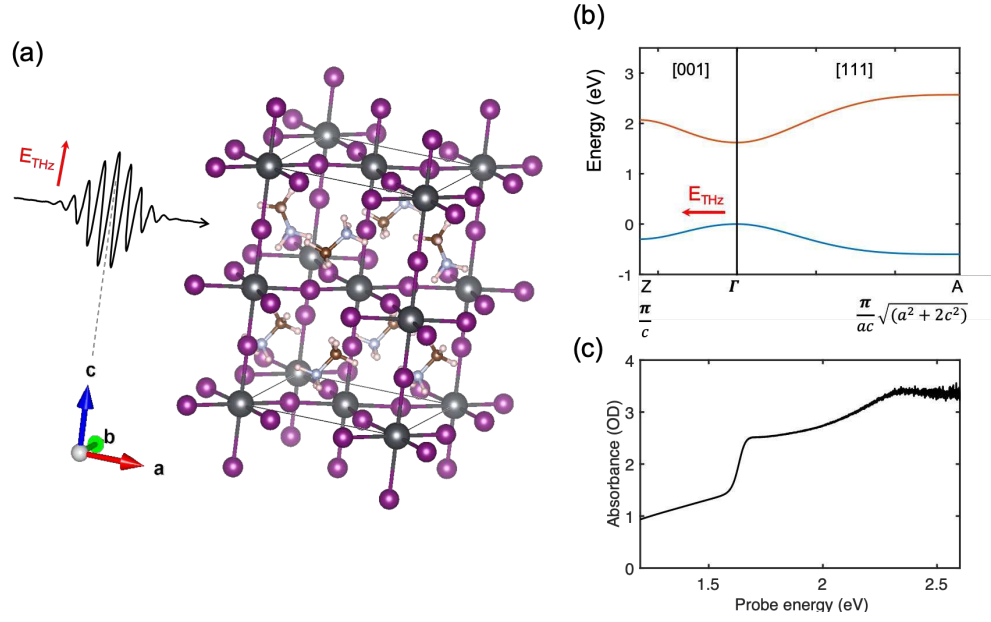


Figure 1. Experimental scheme and properties of MAPbI₃ perovskite (a) THz pulse geometry with a tetragonal unit cell (black rectangular cuboid) of MAPbI₃. (dark grey: Pb, purple: I, brown: C, light blue: N, light pink: H) The THz biasing along the c axis of a crystallite is depicted. (b) Simplified electronic band structure of MAPbI₃ in the tetragonal phase along the directions $\Gamma(0,0,0) \rightarrow Z(0,0,0.5)$ and $\Gamma(0,0,0) \rightarrow A(0.5,0.5,0.5)$. The bandwidths and the lattice parameters are used from [Ref ¹²]. (c) Optical absorption spectrum of MAPbI₃ in the spectral range of the probe pulses.

Results and Discussion

Experimental observation of Wannier-Stark Localization

For applying the strong transient bias, non-resonant in energy with any of the optical phonons and electronic transitions, we employ phase-stable multi-cycle optical pulses with a center frequency of 20 THz. The pump pulse is generated using a difference-frequency generation

scheme in GaSe^{9,10}. For comparison, the MAPbI₃ perovskite has a direct bandgap of $E_{gap} = 1.62$ eV (390 THz, Fig. 1(c)) at room temperature. The phonon modes of Pb-I inorganic sublattice are below 10 THz and methylammonium organic molecular vibrations above 26 THz¹⁴. Due to the presence of the organic cation with a low rotational barrier¹⁵, the crystal shows some degree of disorder at elevated temperature and a less pronounced periodicity compared to all-inorganic perovskites^{15,16}. The sample is a polycrystalline film with a thickness of ~ 300 nm spin-coated^{17,18} on a cyclic olefin/ethylene copolymer substrate (TOPAS[®])¹⁹. The differential transmission induced by the external electric field transient is probed by near-IR and visible probe pulses, with spectra covering broad interband electronic transition energies between 1.4 eV and 2.4 eV (see Fig. S1). The duration of these probe laser pulses is 7 fs, which is significantly shorter than the half-cycle period of the THz pump transients of 25 fs. Details of the experimental settings are described in the Method section and Ref[⁸].

Fig. 2(a) shows the differential transmission $\Delta T/T$ upon applying the THz biasing as a function of delay time between the pump and probe pulses. The peak field strength of the THz pump pulses is 6.1 MV/cm. As expected for the non-resonant THz pulse, the optical response of the material is instantaneous and peaks when the THz field strength is maximal. The modulation occurs at twice the frequency of the THz pulse (Fig. 2(b)), since the measured differential transmission is at least a third-order nonlinear process²⁰. In such a centrosymmetric crystal as the room-temperature tetragonal phase of perovskite MAPbI₃²¹, no contribution from the electro-optic effect is expected which is linear in the electric bias field. The clear temporal modulation of differential transmission appears at high fields, $-100 < \tau < 100$ fs, as the strong E field shortens the interband dephasing time in the vicinity of the bandgap to be comparable to the half-cycle period of 25 fs of the THz

transient. Thus, the precise arrival time of the probe pulse exciting the interband polarization was resolved within the dephasing time.

More importantly, two distinct regimes can be identified in the time-resolved transient spectrum (Fig. 2(a)). For relatively weak fields, $E < 3$ MV, for $\tau < -100$ fs, an induced absorption (blue, $\Delta T/T < 0$) right below and an induced transmission (red, $\Delta T/T > 0$) right above the bandgap of $E_{gap} = 1.62$ eV are observed. The second regime is apparent for field strengths $E > 3$ MV/cm, occurring between delay times $-100 < \tau < 100$ fs (Fig. 2(b)). Here, the maximum modulation depth becomes as large as 38 % at the probe energy of $E_{pr} = 1.7$ eV (Fig. 2(a) and Fig. S2). Also, the transient response covers a significantly extended spectral range, compared to the moderate field regime. The induced transmission (red) above the bandgap now reaches up to $E_{pr} = 1.9$ eV, where it abruptly switches to induced absorption (blue, $\Delta T/T < 0$). This negative region of $\Delta T/T < 0$ persists at probe energies all the way up to $E_{pr} = 2.4$ eV. This one central step from reduced to increased absorption near the center of the band $E_{pr} = 2$ eV, is a noticeable signature of Stark localization, where the Wannier-Stark states are localized onto one unit cell.

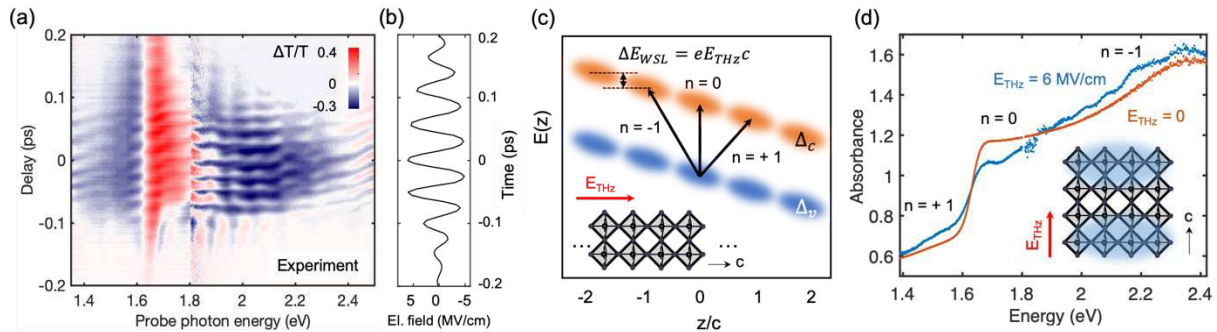


Figure 2. Experimental observation of the transient Wannier Stark localization and the visualized diagram (a) Experimental differential transmission spectra on a polycrystalline film of

MAPbI₃ perovskite at room temperature, as a function of delay time of probe pulses after THz pump pulses. The THz pulses have a peak field strength of 6.1 MV/cm and a center frequency of 20 THz; the probe pulses have photon energy of 1.4 ~ 2.4 eV. (b) Temporal profile of the applied THz bias transient. (c) Schematic picture of Wannier Stark localization. In the presence of strong external fields along the *c* axis, electronic states (orange: conduction band, blue: valence band) are localized to a few layers of *ab* plane, and energetically separated by $\Delta E_{WSL} = eE_{THz}c$ between adjacent lattice sites. Black arrows depict the interband transitions within the same site ($n = 0$) and between different sites ($n = \pm 1$). (d) The absorbance with and without the external transient biasing. The Wannier-Stark localization effectively reduces the 3D electronic structure into 2D layered structure along the *ab* plane, as depicted in blue together with the simplified 3D structure.

By driving the 3-dimensional (3D) system into Wannier-Stark localization, i.e., localizing it in the field direction, we transiently create an effectively 2D electronic system (Fig. 2(c, d)). Given the unit cell doubling, this optically prepared transient 2D system perpendicular to the *c* axis may be directly compared to the physically isolated double-layer structure of PbI₆ octahedra. In such 2D perovskites as (BA)₂(MA)_{l-1}PbI_{3l+1} perovskites²², the inorganic layers (perpendicular to the *c* axis in 3D equivalence) are separated by bulky organic layers²³. The bandgap of the 2D quantum well perovskites is widened due to the bandwidth narrowing (mainly due to the zero dispersion along the vertical direction) compared to 3D perovskite²⁴. In the case of (BA)₂(MA)_{l-1}PbI_{3l+1} perovskites, where the PbI₆ octahedral network forms a double layer ($l = 2$), the optical band gap is ~2.1 eV, which is comparable to the observed 1.9 eV²⁵. It is noteworthy that the observed Wannier-Stark step at $E_{pr} = 1.9$ eV under THz fields is slightly lower than the expected value under static fields due to the spectral broadening induced by the THz modulation, as will be discussed

below. Therefore, the abrupt shift of the absorption edge from $E_{pr} = 1.6$ eV to 1.9 eV at high transient fields (Fig. 2(d)) could be attributed to the transfer of spectral weight from $\alpha(E_{g,3D} < E_{pr} < E_{g,2D})$ to $\alpha(E_{g,2D} < E_{pr})$. Such a THz-induced reduction of dimensionality from a 3D to a 2D system could enable new applications in both transport and optoelectronics due to the relatively easy access to that regime in these hybrid perovskite materials.

Simulations considering one orientation

To capture the essential ingredients responsible for the experimental observations, we carry out theoretical calculations based on different models of increasing complexity. We start with considering perfect alignment of the THz field with the direction along which the joint bandwidth of the highest valence and the lowest conduction band is narrowest. For the case of the tetragonal MAPbI₃ perovskite, the narrowest joint bandwidth, $\Delta_{\overline{\Gamma Z}} = 0.75$ eV, is along the $\overline{\Gamma Z}$ direction (Fig. 1(b))¹². We thus take into account two one-dimensional bands, i.e., one valence and one conduction band with a cosine-like (tight-binding) band structure and the bandgap of 1.62 eV. Thus, the energy difference for interband transitions is taken as $E_{cv}(k) = 1.62$ eV + $(\Delta_{\overline{\Gamma Z}}/2)(1 - \cos(g(k, a^*)ka^*))$ (see Methods section for details of the function $g(k, a^*)$). For this model, the spectra are obtained by numerically solving the semiconductor Bloch equations^{26–28}, as described in the Methods section.

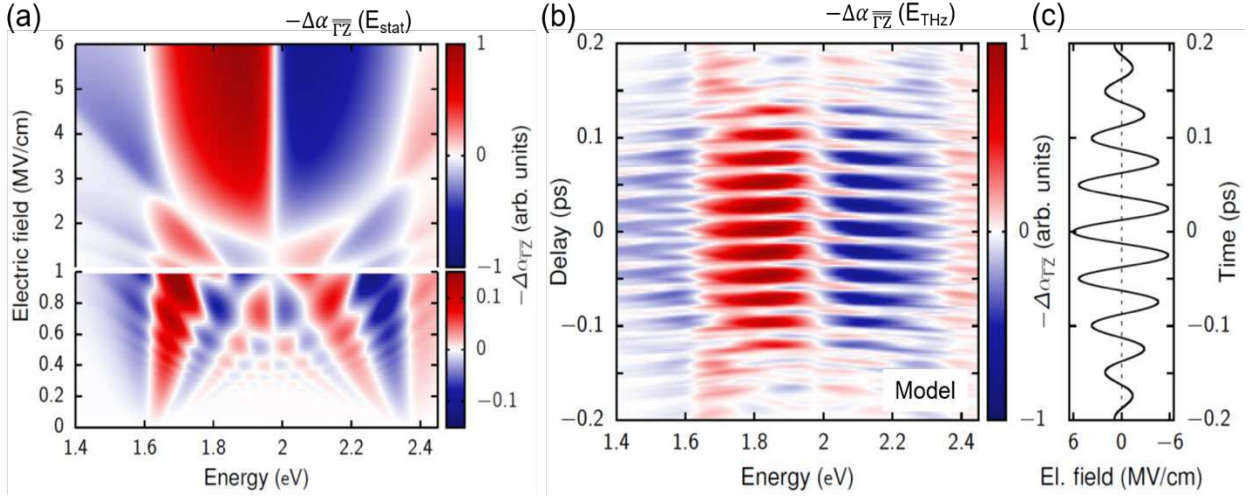


Figure 3. Numerical simulation of differential absorption spectra (a) Negative change of the optical interband absorption $-\Delta\alpha_{\Gamma Z}$ for static fields from a cosine band modeling along ΓZ direction. The region of electric field strengths up to 1 MV/cm is enlarged to show Franz-Keldysh oscillations and the transition to the Wannier-Stark regime. (b) Calculated $-\Delta\alpha_{\Gamma Z}$ spectra for the excitation with a THz pulse with a peak field strength of $E_0 = 6$ MV/cm, where the delay τ between the THz and the optical pulse is varied. (c) Simulated temporal profile of the applied THz bias transient. The pulse duration \bar{T} is 240 fs, the THz frequency is 20 THz, and the dephasing time is $T_2 = 20$ fs.

Already when considering static fields (Fig. 3(a)), the simulation results obtained by this simple model exhibits substantial qualitative similarities with the transient experimental results shown in Fig. 2(a). For all field strengths, increased absorption is present below the bandgap and reduced absorption directly above the band gap. For rather weak field strengths of up to about 0.5 MV/cm, oscillations arising from the Franz-Keldysh effect are visible, shifting towards the band center with

increasing field. For fields exceeding ~ 3 MV/cm, signatures of Wannier-Stark localization become noticeable, as the field-dependent interband transition energies shift to higher and lower energies by $neED$ with increasing E (Fig. 2(c)). Starting at around 3 MV/cm, the condition for Stark localization is fulfilled, i.e., $eED > \Delta/2$ (meaning that the energy of the ($n = -1$) Wannier-Stark state is in the bandgap region, see Fig. 2(c, d)), and therefore, the dominant feature is the step-like change from reduced absorption to induced absorption in the center of the band at 1.974 eV (this value is the average transition frequency within our model). This step-like change is, in fact, also the main feature visible in the experimental results for sufficiently high fields, i.e., between about $-100 < \tau < 100$ fs as shown in Figs. 2 (a).

Besides, by considering pulsed THz fields, the simulated differential spectra with the same model (Fig. 3(b, c)) well describe both spectral and temporal features in the observed transient modulation of differential transmission spectra (Fig. 2(a)). Fig. 3(b) shows the negative change of the transient absorption, $-\Delta\alpha_{\overline{TZ}}$, upon non-resonant biasing with a THz pulse with a peak field strength of $E_0 = 6$ MV/cm and a center frequency of 20 THz, as shown in Fig. 3(c). Besides temporal modulation of the entire transient spectra at twice the carrier frequency of the THz transient, the dominant feature at sufficiently large field strengths ($-100 < \tau < 100$ fs) is the rapid change from increased to reduced transmission in the center of the band $E_{pr} = 2$ eV, which originates from Stark localization. The slightly lower value of the observed central step at $E_{pr} = 1.9$ eV and the asymmetric nature of the spectral shape with respect to the central step (Fig. 2(a)) compared to this simplified model (Fig. 3 (b)) can be explained by the polycrystallinity of the system as discussed below. Given the complexity, disorder, and polycrystallinity of the investigated sample, the required field strength at which this step starts to appear is in surprisingly good agreement with the experiment which confirms that the observed response constitutes a clear

sign of Wannier-Stark localization. Our interpretations are further supported by Fig. S6, which shows how the results of Fig. 3 change if we consider that the THz field is aligned with the $\overline{\Gamma A}$ direction instead of the $\overline{\Gamma Z}$ direction. Comparing those two figures clearly shows that due to the larger bandwidth in the $\overline{\Gamma A}$ direction the Wannier-Stark localization requires higher field amplitudes to develop and furthermore would lead to a transition from reduced to induced absorption at significantly higher energies as observed in experiment. The effects of different field directions and the averaging over them is discussed in more detail below (see Fig. 4).

As demonstrated so far, Wannier-Stark localization starts to occur at the field amplitude as low as 3 MV/cm in the MAPBI₃ perovskite, due to the relatively large periodicity, the narrow joint bandwidth, and the coincidence of the two along the same direction. The largest lattice constant of tetragonal MAPBI₃ perovskite, along the c axis, $c = 12.5 \text{ \AA}$, is more than twice as large as those of conventional all-inorganic semiconductors crystallizing with strong covalent bonds in the diamond, wurtzite, or zincblende forms (3.5 ~ 6.5 \AA at 300 K). This finding arises because (i) the cubic perovskite unit cell is expanded through rotation of ab plane by 45° and cell doubling along c axis in the tetragonal phase; and (ii) the pseudocubic lattice parameter formed by relatively large Pb²⁺ and I⁻ ions is 6.3 \AA ¹³, which is at the larger side of the distribution of parameters for cubic lattice parameters. The pseudocubic lattice parameter is large enough to accommodate large organic molecular cations within the void of their network.

The direction of the narrowest joint bandwidth of the conduction and valence bands, $\overline{\Gamma Z}$, coincides with the c axis. The conduction band is composed of the overlap of Pb(6p)-I(5p) atomic orbitals and the valence band is of that of Pb(6s)-I(5p) orbitals²⁹. Thus, the Pb-I bond length as well as the Pb-I-Pb angle could determine the widths of both bands and the magnitude of the band

gap. In the tetragonal MAPbI₃ perovskite, the corner-shared PbI₆ octahedra in cubic phase are tilted about the c axis in the opposite direction between successive tilts, which reduces the Pb-I-Pb angle from 180° along the diagonal direction of the a and b axis. The smaller Pb-I-Pb bond angle indicates weaker orbital overlap between Pb and I atoms and thus smaller band dispersion along $\overline{\Gamma M}$ than $\overline{\Gamma Z}$. However, the Pb-I bond lengths along the c axis is known to be longer on average³⁰ and has greater effect on the dispersion than the angle due to the σ bonding nature, which leads to the coincidence of the direction of the largest lattice constant and the narrowest bandwidth. We note that unlike GaAs, the body diagonal direction exhibits the strongest dispersion ($\overline{\Gamma A}$). Overall, the large ionic diameter and the geometric distortion result in the unusually narrow joint bandwidth, lower than 1 eV.

Including polycrystallinity by averaging over orientations

We now account for the system's polycrystallinity by considering contributions to the differential transmittance spectra from crystallites with orientations different from those with the c axis parallel to the THz field polarization. To include arbitrary orientations of the crystallites into our simulations, we take the $\overline{\Gamma Z}$ and the $\overline{\Gamma A}$ directions, i.e., the two extreme directions with the narrowest/broadest bandwidth and simultaneously the smallest/largest distance in k -space (see Fig. 1(b)) and perform an average overall in between bandwidths and extensions of the first Brillouin zone (see Method section), by interpolating between the two limiting cases with a parameter f . The simulated absorption changes at a field amplitude of $E_0 = 4$ MV/cm with various interpolation parameters f 's are shown in Fig. 4 (a) together with the measured differential spectra at different instantaneous field amplitudes of the THz pulse (Fig. 4 (b)). Here, $f = 0$ denotes the response along the $\overline{\Gamma Z}$ direction (i.e., the c -axis), and $f = 1$ along the $\overline{\Gamma A}$ direction.

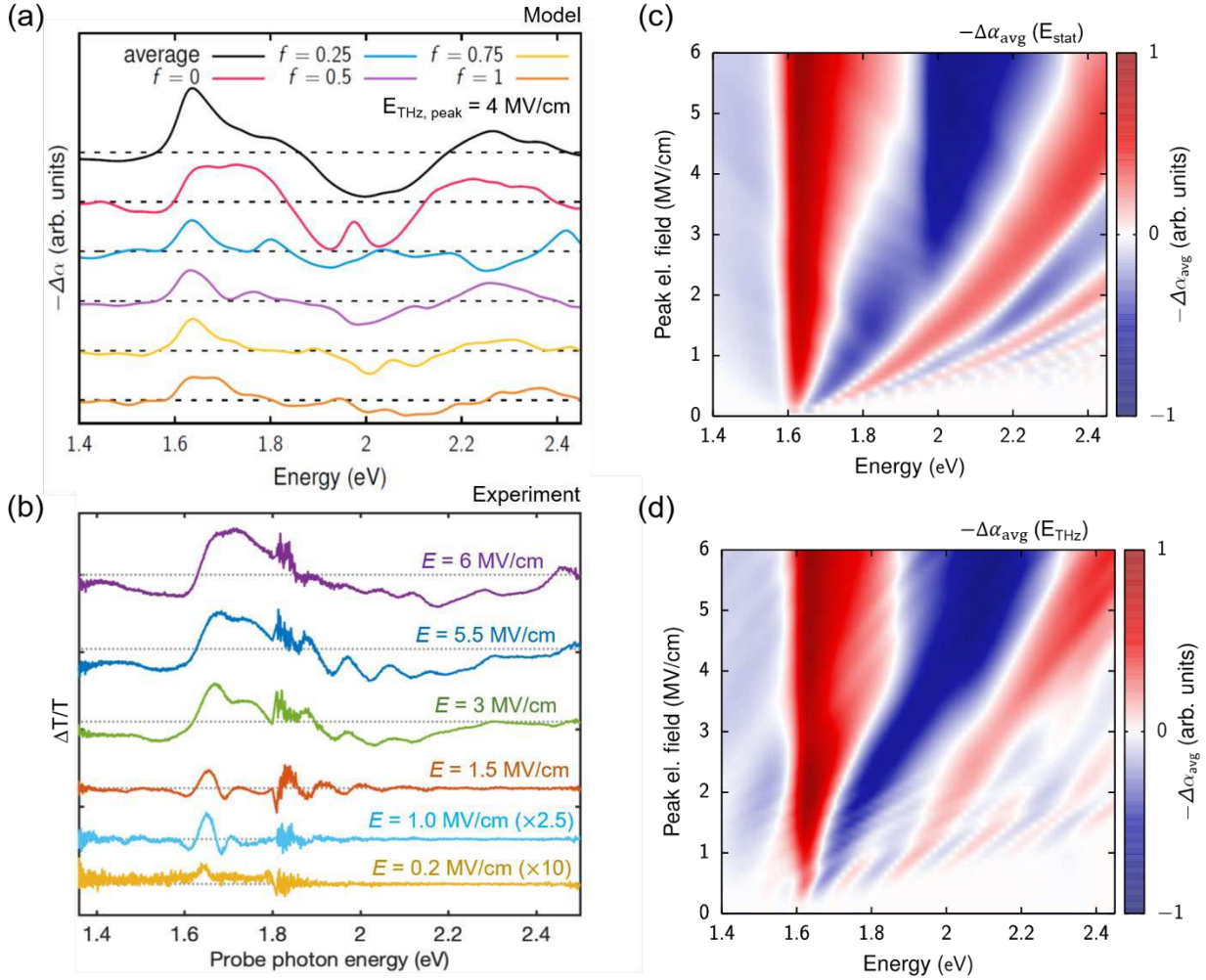


Figure 4. Experiments on polycrystalline system and simulations with averaging of cosine band model from ΓZ to ΓA direction. (a) Illustration for the averaging process over the interpolation parameter f from the $\bar{\Gamma Z}$ direction ($f = 0$) to $\bar{\Gamma A}$ direction ($f = 1$). The negative absorption changes $-\Delta\alpha_f$ are calculated for different one-dimensional systems using a THz pulse centered at $t = 0$, with an amplitude of $E_0 = 4$ MV/cm, a pulse duration of $\bar{T} = 240$ fs, and a THz center frequency of 20 THz. (b) Temporal slices of $\Delta T/T$ as a function of probe photon energy (Fig. 2(a)), at a delay time corresponding to the contour with constant electric field amplitudes E (Fig. 2(b)). (c) averaged absorption change, $-\Delta\alpha_{\text{avg}}$, for static fields of various strengths. (d) averaged absorption change, $-\Delta\alpha_{\text{avg}}$, for a THz pulse centered at $t = 0$ and various field strengths.

As shown in Fig. 4(a), the absorption changes depend strongly on the interpolation parameter f , i.e., on the bandwidth and the distance to the border of the first Brillouin zone. For $f = 0$, which corresponds to the $\overline{\Gamma Z}$ direction, the field amplitude of $E_0 = 4$ MV/cm drives the system into the region of Stark localization. Therefore, for a static field of such an amplitude, one would see a strong induced absorption in the band center at 1.974 eV, which corresponds to an optical transition to the Stark localized state. The transient nature of the THz pulse causes the single negative peak to be split into two peaks and the spectral region of induced absorption to be slightly broadened. With increasing f , both the bandwidth and the distance to the border of the first Brillouin zone increase. As a result, the minimum field strength for which Stark localization is realized increases significantly by approximately a factor $(c/a_{\overline{\Gamma Z}}^*)(\Delta_{\overline{\Gamma A}}/\Delta_{\overline{\Gamma Z}})$, equaling about 4.7. Consequently, already for $f = 0.25$, the absorption changes show no sign of Stark localization, with several oscillations emerging owing to the THz driving. This trend of overall weaker absorption changes with some oscillatory structure is also present for even larger f . The only feature present in all spectra shown in Fig. 4 (a) is some induced absorption below the bandgap and reduced absorption directly above the bandgap.

However, when averaging over the interpolation parameter f , i.e., over the orientations considered by our modeling, the result (black curve in Fig. 4(a)) reproduces the main features present for $f = 0$, with somewhat fewer oscillations. Most importantly, the change from bleaching to induced absorption in the center of the band structure for the $\overline{\Gamma Z}$ direction at about 1.9 eV is still present. The averaged graph is in good agreement with the differential spectra at high field amplitudes (upper curves in Fig. 4(b)). Thus, in the averaged results, the spectra for small f

dominate strongly since (i) the absorption changes are spectrally concentrated in the monitored region due to the small bandwidth, (ii) one is in the regime of Stark localization due to the small extent of the first Brillouin zone, and (iii) for larger f the rather weak and oscillatory results partly cancel each other. For these reasons, the contribution from the $\overline{\Gamma Z}$ direction, corresponding to small f , is enhanced for energies far above the bandgap and dominates the entire phenomenon.

The results of Fig. 4(a, b) suggest that, for the randomly oriented crystallites in the film, the overall response is dominated by the response originating from the band dispersion in the $\overline{\Gamma Z}$ direction. This reasoning is substantiated by the averaged field-dependent absorption changes calculated for both a static and a THz field shown in Figs. 4(c) and (d), respectively. As expected, the $\overline{\Gamma Z}$ direction dominates the averaged results, which include the contributions from the dispersion in all the other directions. In both cases for strong fields, the dominant feature is a rapid change from reduced to increased absorption, which takes place near the center of the interband absorption that corresponds to the dispersion in the $\overline{\Gamma Z}$ direction. Due to the spectral broadening induced by the THz modulation, this transition appears at slightly lower photon energies for the THz field, Fig. 4(c), than for the static field, Fig. 4(d). Thus, Fig. 4(c, d) is consistent with the notion that the step-like sign change in the center of the band for sufficiently strong field amplitudes is a signature of Stark localization for the polycrystalline perovskite sample.

In conclusion, we have demonstrated the onset of transient Wannier-Stark localization in the polycrystalline form of methylammonium lead iodide perovskite at surprisingly low electric field amplitudes. Despite the static and dynamic disorder of the methylammonium molecular cations at room temperature and the arbitrary distribution of crystal domains with respect to the THz field direction, the dominant contribution from the $\overline{\Gamma Z}$ direction of the band structure allows for the clear

signature of Wannier-Stark localization. The ultrafast field-induced transition from 3D to effectively 2D electronic states leads to substantial spectral transfer from the central spatially-direct ($n = 0$) transition (around the optical band gap of 3D) to 0.3 eV red- (blue-)shifted spatially adjacent transitions $n = +1$ ($n = -1$), with up to 38 % maximum modulation depth. Instead of semiconductor superlattices, which need expensive high-vacuum manufacturing processes, the solution-processed hybrid perovskites could meet the growing need for cost-effective³¹, efficient, fast, and sensitive characteristics as optical modulators³². Together with the renowned photophysical properties of MAPbI₃, such as the long carrier diffusion length^{33,34}, low mid-gap trap density^{29,34}, and large absorption coefficient³⁵, this finding of high modulation depth, fast response, and low onset field for Wannier-Stark localization highlights the potential of this material in photonic applications^{36,37}.

Materials and Methods

Experimental details

The phase-stable multi-cycle mid-IR pulses with a peak field strength of ~ 10 MV/cm are generated using difference frequency mixing (DFG) in GaSe^{9,10}. The regeneratively amplified pulses with 780 nm and 130 fs are used to pump two parallel optical parametric amplifier stages to provide tunable near-infrared pulses with minimum relative phase fluctuation. The two near-IR pulses are then combined and sent to the GaSe nonlinear crystal for the DFG. The thus generated mid-IR pulses are focused onto the sample with off-axis parabolic mirrors of focal length $\tilde{f} = 15$ mm and effective NA = 0.2. The electric field transient is characterized by ultrabroadband electro-optic sampling³⁸ at a 30- μ m-thick GaSe crystal using balanced detection of an 8-fs probe pulse centered at a wavelength of 1.2 μ m as the gating pulse. The quantitative value of the field

amplitude is obtained by measuring the mid-IR average power and focal spot size. Then, the value at the interior of the MAPbI₃ perovskite sample are estimated using the Fresnel transmission coefficient for the mid-IR field at the air–MAPbI₃ interface.

For detection of the field-induced differential optical transmittance in broad spectral range, we generate near-IR and visible pulses with the duration of 7 fs by non-collinear optical parametric amplification (Fig. S1)³⁹. The probe pulses are combined with the mid-IR pump pulses at a germanium beam splitter so that both pulses co-propagate through the sample. The probe pulses are then dispersed onto a spectrometer coupled to a CCD camera for the spectral resolution. The relative timing between the pump and probe pulses was controlled using an optical delay stage. To detect the differential optical transmission spectra, we modulate the mid-IR pump pulses by an optical chopper operating at 125 Hz, which is synchronized with the 1 kHz laser repetition rate and the readout of the CCD camera. Two subsequent spectra taken from the CCD camera are subtracted by each other and normalized by one spectrum without the pump. The sample compartment in the experimental setup was purged with dry nitrogen in order to avoid degradation. The complete experimental setup and the laser system have been fully illustrated in Ref [8].

Theoretical approach

For calculating the linear optical interband absorption spectra, we numerically solve the semiconductor Bloch equations (SBE), including the intraband acceleration induced by the strong THz field^{26–28}. We use here a one-dimensional trajectory in k-space, denoted as the $\overline{\Gamma x}$ direction where x is an arbitrary point in the 1. Brillouin zone, which is parallel to the polarization direction

of the incident THz field and goes through the Γ -point of the Brillouin zone. In the linear optical regime, the SBE reduce to the equations of motion for the microscopic polarizations p_k^{cv} and read

$$\frac{\partial}{\partial t} p_k^{cv} = \frac{i}{\hbar} E_{cv}(k) p_k^{cv} + \frac{e}{\hbar} E_{\text{THz}}(t) \nabla_k p_k^{cv} - \frac{i}{\hbar} E_{\text{opt}}(t) \mu_k^{vc} - \frac{p_k^{cv}}{T_2}$$

Dephasing processes are treated phenomenologically by adding the dephasing time T_2 .

For all calculations presented in this paper, we include the intraband dynamics induced by the static or pulsed THz fields to infinite order, whereas the weak optical probe of the interband absorption is considered only to the first order. In this linear-optical regime, we thus neglect carrier generation by multi-photon processes and impact ionization, which does not seem to play a dominant role in the measured transient spectra. Interband tunneling by the THz field could lead to bleaching at later delay times and the slightly asymmetric spectral evolution with respect to $\tau = 0$ (Fig. 2(A)) (corresponding to the trailing edge of the THz transient in the Supplementary Material of ref [8]). However, significant carrier multiplication does not occur within this experimental window, as shown in Fig. S3.

For the interband dipole matrix element, we use the usual decay with increasing transition frequency⁴⁰

$$\mu_k = \mu_0 \frac{1.62 \text{ eV}}{E_{cv}(k)}$$

where the choice of μ_0 is not relevant here, as it contributes only as a prefactor to the absorption spectra.

For the THz pulses, we use a Gaussian envelope

$$E_{\text{THz}}(t) = E_0 e^{-4 \ln(2) \left(\frac{t-\tau}{\bar{T}}\right)^2} \cos(\omega_{\text{THz}}(t - \tau))$$

with the electric-field amplitude E_0 , the pulse duration \bar{T} (FWHM of the intensity), the time delay τ , and the THz frequency ω_{THz} . The optical probe pulse is modeled as a weak ultrashort delta-like pulse.

The total optical polarization is obtained by summing over the microscopic polarizations p_k^{cv}

$$P(t) = \sum_k \mu_k^* p_k^{cv}(t) + c. c.$$

By Fourier transforming the macroscopic polarization $P(t)$ the linear absorption can be obtained by

$$\alpha_{1\text{D},\bar{\Gamma}_x}(\omega) \propto \omega \text{Im}(P(\omega))$$

To be able to compare the numerical results for the one-dimensional k-space trajectory to the measured $\Delta T/T$ spectra, the negative change of the optical absorption in three dimensions $-\Delta\alpha_{3\text{D}}$ is calculated assuming a parabolic electronic dispersion perpendicular to the considered one-dimensional direction. Due to the constant two-dimensional density of states for a parabolic dispersion, the absorption of the corresponding three-dimensional system is easily obtained as Ref [8]

$$\alpha_{\bar{\Gamma}_x}(\omega) \propto \int_0^\omega \alpha_{1\text{D},\bar{\Gamma}_x}(\omega') d\omega' .$$

Band structure model and averaging over crystallographic directions

To incorporate both the bandwidth and the effective mass m^* at the band gap as obtained from ab-initio calculation in Ref [12] into our model, we use an interband energy difference of

$$E_{cv}(k) = E_0 + \frac{\Delta}{2}(1 - \cos(g(ka^*)ka^*))$$

Here, π/a^* is the distance from the Γ -point to the border of the first Brillouin zone

and the interpolation function

$$g(ka^*) = f + (1 - f) \frac{ka^*}{\pi}$$

guarantees that $E_{cv}(0) = E_0$ and $E_{cv}(\pm\pi/a^*) = E_0 + \Delta$, meaning the bandgap energy E_0 and the bandwidth Δ are preserved.

The parameter f is adjusted to obtain the effective mass which corresponds to the second derivative of the band structure at the Γ point:

$$m^* = \hbar^2 \left[\frac{d^2 E_{cv}(k)}{dk^2} \Big|_0 \right]^{-1}$$

as given in Ref [12].

As mentioned before, the polycrystallinity of the system is included by averaging over several differential transmittance spectra.

The transition from the $\overline{\Gamma Z}$ to the $\overline{\Gamma A}$ direction is carried out by varying the bandwidth Δ from $\Delta_{\overline{\Gamma Z}} = 0.75$ eV to $\Delta_{\overline{\Gamma A}} = 1.55$ eV, the extent of the first Brillouin zone $\frac{\pi}{a^*}$ from $\frac{\pi}{a_{\overline{\Gamma Z}}^*} = \frac{\pi}{c} = \frac{\pi}{1.27} \text{ nm}^{-1}$

to $\frac{\pi}{a_{\Gamma\bar{A}}^*} = \frac{\pi}{a c} \sqrt{2c^2 + a^2} = \frac{\pi}{0.56} \text{ nm}^{-1}$ and the effective mass m^* from $m_{\Gamma\bar{Z}}^* = 0.17m_0$ to $m_{\Gamma\bar{A}}^* = 0.09m_0$ via a parameter f which varies from 0 (i.e. the $\Gamma\bar{Z}$ -direction) to 1 (i.e. the $\Gamma\bar{A}$ -direction)

¹². The interpolation is performed as:

$$\Delta(f) = \Delta_{\Gamma\bar{Z}} + f(\Delta_{\Gamma\bar{A}} - \Delta_{\Gamma\bar{Z}})$$

$$\frac{\pi}{a^*(f)} = \frac{\pi}{a_{\Gamma\bar{Z}}^*} + f \left(\frac{\pi}{a_{\Gamma\bar{A}}^*} - \frac{\pi}{a_{\Gamma\bar{Z}}^*} \right)$$

$$m^*(f) = m_{\Gamma\bar{Z}}^* + f(m_{\Gamma\bar{A}}^* - m_{\Gamma\bar{Z}}^*)$$

where $f=0$ describes the $\Gamma\bar{Z}$ -direction and $f=1$ the $\Gamma\bar{A}$ -direction, respectively.

The above described averaging of several spectra for the discretized parameter f is performed via evaluating

$$\alpha_{\text{avg}}(\omega) = \frac{1}{n} \sum_{f_i} \alpha_{f_i}(\omega), i \in [1, n]$$

With the respective absorption $\alpha_{f=0} = \alpha_{1D,\Gamma\bar{Z}}$ and $\alpha_{f=1} = \alpha_{1D,\Gamma\bar{A}}$ where for convergence n is typically chosen as 51.

Supporting Information

Fig. S1. Normalized spectra of near-IR (red) and visible (blue) probe pulses.

Fig. S2. Differential transmission changes measured at probe photon energies of 1.7 eV (red line) and 2.0 eV (blue) together with the $E^2(t)$ of THz pulse profile.

Fig. S3. Contributions from free carriers generated via interband tunneling.

Fig. S4. Simulations with averaging from the $\bar{\Gamma Z}$ to the $\bar{\Gamma A}$ direction for a THz pulse centered at $t = 0$ and various field strengths.

Fig. S5. Simulated absorption change, $-\Delta\alpha_{\text{avg}}$, averaged for a pure cosine model band structure (without the function g , see methods, which was introduced to fit the effective mass) from $\bar{\Gamma Z}$ to $\bar{\Gamma A}$ direction for a THz pulse centered at $t = 0$ and various field strengths.

Figure S6. Simulated change of the optical interband absorption $-\Delta\alpha_{\bar{\Gamma A}}$ from a cosine band modeling along $\bar{\Gamma A}$ direction for static fields and a pulsed THz field.

AUTHOR INFORMATION

Corresponding Author

*Corresponding author. torsten.meier@upb.de; kim@mpip-mainz.mpg.de

Author Contributions

The manuscript was written through contributions of all authors. All authors have given approval to the final version of the manuscript. ‡These authors contributed equally.

Notes

The authors declare no competing financial interest.

ACKNOWLEDGMENT

The authors thank Keno Krewer and Johannes Hunger for helpful discussions. T. M. and D. B. acknowledge financial support from the Deutsche Forschungsgemeinschaft (DFG, German Research Foundation) through the Collaborative Research Center TRR 142 (project number 231447078, project A02). M. B. and H. K. thank the DFG for financial support through the Collaborative Research Center TRR 288 (project number 422213477, project B07), the European Union's Horizon 2020 research and innovation program under grant agreement No.658467, and the Max Planck Society for financial support. A. L. and J. B. acknowledge financial support from the European Research Council through ERC Advanced Grant 290876 (UltraPhase) and the Carl Zeiss Foundation through the fellowship program.

REFERENCES

1. Wannier, G. H. Wave Functions and Effective Hamiltonian for Bloch Electrons in an Electric Field. *Phys. Rev.* **117**, 432–439 (1960).
2. Bloch, F. Über die Quantenmechanik der Elektronen in Kristallgittern. *Zeitschrift für Phys.* **52**, 555–600 (1929).
3. Zener, C. A theory of the electrical breakdown of solid dielectrics. *Proc. R. Soc. London. Ser. A* **145**, 523–529 (1934).
4. Mendez, E. E., Agulló-Rueda, F. & Hong, J. M. Stark Localization in GaAs-GaAlAs Superlattices under an Electric Field. *Phys. Rev. Lett.* **60**, 2426–2429 (1988).
5. Voisin, P. *et al.* Observation of the Wannier-Stark Quantization in a Semiconductor

- Superlattice. *Phys. Rev. Lett.* **61**, 1639–1642 (1988).
6. Feldmann, J. *et al.* Optical investigation of Bloch oscillations in a semiconductor superlattice. *Phys. Rev. B* **46**, 7252–7255 (1992).
 7. Waschke, C. *et al.* Coherent submillimeter-wave emission from Bloch oscillations in a semiconductor superlattice. *Phys. Rev. Lett.* **70**, 3319–3322 (1993).
 8. Schmidt, C. *et al.* Signatures of transient Wannier-Stark localization in bulk gallium arsenide. *Nat. Commun.* **9**, (2018).
 9. Sell, A., Leitenstorfer, A. & Huber, R. Phase-locked generation and field-resolved detection of widely tunable terahertz pulses with amplitudes exceeding 100 MV/cm. *Opt. Lett.* **33**, 2767 (2008).
 10. Junginger, F. *et al.* Single-cycle multiterahertz transients with peak fields above 10 MV/cm. *Opt. Lett.* **35**, 2645 (2010).
 11. von Plessen, G. *et al.* Influence of scattering on the formation of Wannier-Stark ladders and Bloch oscillations in semiconductor superlattices. *Phys. Rev. B* **49**, 14058–14061 (1994).
 12. Umari, P., Mosconi, E. & De Angelis, F. Relativistic GW calculations on CH₃ NH₃ PbI₃ and CH₃ NH₃ SnI₃ Perovskites for Solar Cell Applications. *Sci. Rep.* **4**, 1–7 (2014).
 13. Whitfield, P. S. *et al.* Structures, Phase Transitions and Tricritical Behavior of the Hybrid Perovskite Methyl Ammonium Lead Iodide. *Sci. Rep.* **6**, 1–16 (2016).
 14. Brivio, F. *et al.* Lattice dynamics and vibrational spectra of the orthorhombic, tetragonal, and cubic phases of methylammonium lead iodide. *Phys. Rev. B* **92**, 1–8 (2015).

15. Quarti, C., Mosconi, E. & De Angelis, F. Interplay of orientational order and electronic structure in methylammonium lead iodide: Implications for solar cell operation. *Chem. Mater.* **26**, 6557–6569 (2014).
16. Leguy, A. M. A. *et al.* Dynamic disorder, phonon lifetimes, and the assignment of modes to the vibrational spectra of methylammonium lead halide perovskites. *Phys. Chem. Chem. Phys.* **18**, 27051–27066 (2016).
17. Kim, H. *et al.* Direct observation of mode-specific phonon-band gap coupling in methylammonium lead halide perovskites. *Nat. Commun.* **8**, 687 (2017).
18. Karakus, M. *et al.* Phonon-Electron Scattering Limits Free Charge Mobility in Methylammonium Lead Iodide Perovskites. *J. Phys. Chem. Lett.* **6**, 4991–4996 (2015).
19. D’Angelo, F., Mics, Z., Bonn, M. & Turchinovich, D. Ultra-broadband THz time-domain spectroscopy of common polymers using THz air photonics. *Opt. Express* **22**, 12475–12485 (2014).
20. Yan, W. X., Zhao, X. G. & Wang, H. Coherent effects induced by dc-ac fields in semiconductor superlattices: The signature of fractional Wannier-Stark ladders. *J. Phys. Condens. Matter* **10**, L11 (1998).
21. Frohna, K. *et al.* Inversion symmetry and bulk Rashba effect in methylammonium lead iodide perovskite single crystals. *Nat. Commun.* **9**, (2018).
22. Blancon, J. C. *et al.* Unusual thickness dependence of exciton characteristics in 2D perovskite quantum wells. *arXiv:1710.07653v2*

23. Ishihara, T. & Goto, T. Exciton Features in 0-, 2-, and 3-Dimensional Networks of [PbI₆]⁴⁻ Octahedra. *Journal of the Physical Society of Japan* **63**, 3870–3879 (1994).
24. Umebayashi, T. *et al.* Electronic structures of lead iodide based low-dimensional crystals. *Phys. Rev. B* **67**, 2–7 (2003).
25. Blancon, J. C. *et al.* Unusual thickness dependence of exciton characteristics in 2D perovskite quantum wells. *arXiv* 1–21 (2017).
26. Schubert, O. *et al.* Sub-cycle control of terahertz high-harmonic generation by dynamical Bloch oscillations. *Nat. Photonics* **8**, 119–123 (2014).
27. Meier, T., Von Plessen, G., Thomas, P. & Koch, S. W. Coherent electric-field effects in semiconductors. *Phys. Rev. Lett.* **73**, 902–905 (1994).
28. Golde, D., Meier, T. & Koch, S. W. High harmonics generated in semiconductor nanostructures by the coupled dynamics of optical inter- and intraband excitations. *Phys. Rev. B* **77**, 1–6 (2008).
29. Brandt, R. E., Stevanović, V., Ginley, D. S. & Buonassisi, T. Identifying defect-tolerant semiconductors with high minority-carrier lifetimes: Beyond hybrid lead halide perovskites. *MRS Commun.* **5**, 265–275 (2015).
30. Guo, L., Xu, G., Tang, G., Fang, D. & Hong, J. Structural stability and optoelectronic properties of tetragonal {MAPbI₃} under strain. *Nanotechnology* **31**, 225204 (2020).
31. Ball, J. M., Lee, M. M., Hey, A. & Snaith, H. J. Low-temperature processed meso-structured to thin-film perovskite solar cells. *Energy Environ. Sci.* **6**, 1739 (2013).

32. Grinblat, G. *et al.* Ultrafast All-Optical Modulation in 2D Hybrid Perovskites. *ACS Nano* **13**, 9504–9510 (2019).
33. Stranks, S. D. *et al.* Electron-hole diffusion lengths exceeding 1 micrometer in an organometal trihalide perovskite absorber. *Science* **342**, 341–4 (2013).
34. Shi, D. *et al.* Low trap-state density and long carrier diffusion in organolead trihalide perovskite single crystals. *Science* **347**, 519–522 (2015).
35. Lee, M. M., Teuscher, J., Miyasaka, T., Murakami, T. N. & Snaith, H. J. Efficient hybrid solar cells based on meso-superstructured organometal halide perovskites. *Science* **338**, 643–7 (2012).
36. Bar-Joseph, I. *et al.* Room-temperature electroabsorption and switching in a GaAs/AlGaAs superlattice. *Appl. Phys. Lett.* **55**, 340–342 (1989).
37. Bigan, E. *et al.* Optimization of optical waveguide modulators based on Wannier-Stark localization: an experimental study. *IEEE J. Quantum Electron.* **28**, 214–223 (1992).
38. Riek, C., Seletskiy, D. V & Leitenstorfer, A. Femtosecond measurements of electric fields: from classical amplitudes to quantum fluctuations. *Eur. J. Phys.* **38**, 24003 (2017).
39. Brida, D. *et al.* Few-optical-cycle pulses tunable from the visible to the mid-infrared by optical parametric amplifiers. *J. Opt.* **12**, 13001 (2009).
40. Haug, H. & Koch, S. W. *Quantum Theory of the Optical and Electronic Properties of Semiconductors.* (WORLD SCIENTIFIC, 2009).

Figures

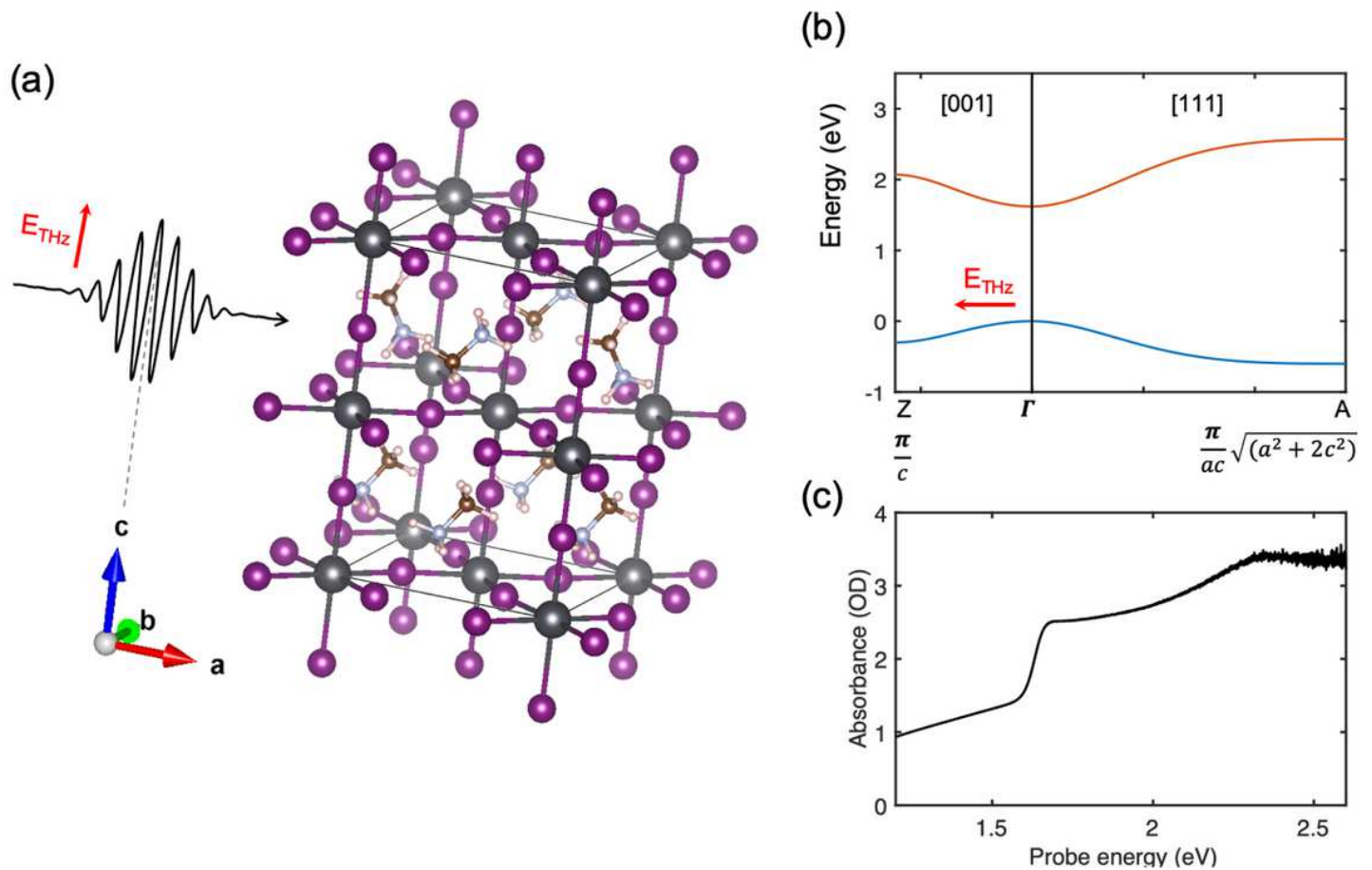


Figure 1

Experimental scheme and properties of MAPbI₃ perovskite (a) THz pulse geometry with a tetragonal unit cell (black rectangular cuboid) of MAPbI₃. (dark grey: Pb, purple: I, brown: C, light blue: N, light pink: H) The THz biasing along the c axis of a crystallite is depicted. (b) Simplified electronic band structure of MAPbI₃ in the tetragonal phase along the directions $\Gamma(0,0,0) \rightarrow Z(0,0,0.5)$ and $\Gamma(0,0,0) \rightarrow A(0.5,0.5,0.5)$. The bandwidths and the lattice parameters are used from [Ref 12]. (c) Optical absorption spectrum of MAPbI₃ in the spectral range of the probe pulses.

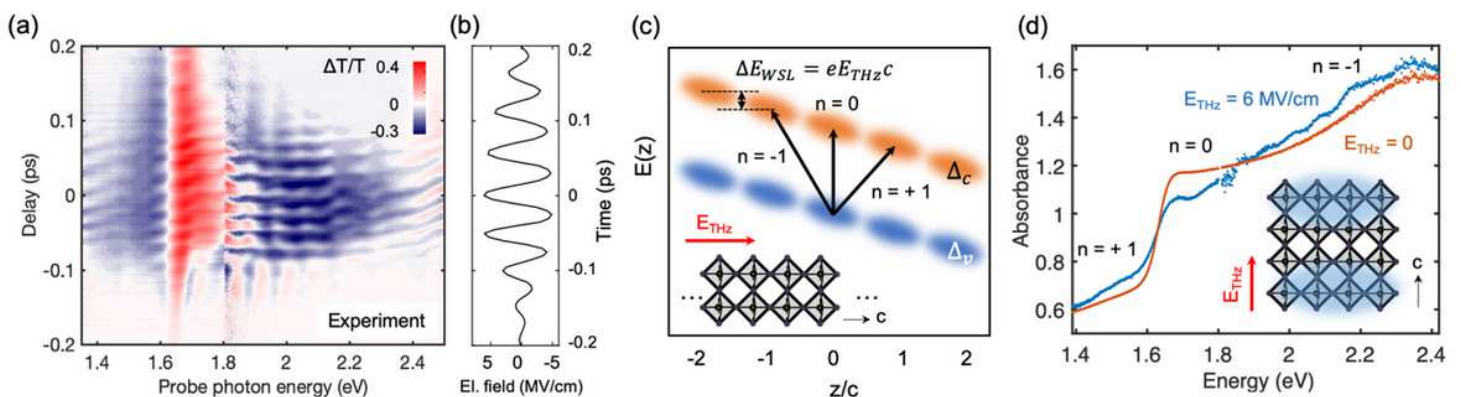


Figure 2

Experimental observation of the transient Wannier Stark localization and the visualized diagram (a) Experimental differential transmission spectra on a polycrystalline film of MAPbI₃ perovskite at room temperature, as a function of delay time of probe pulses after THz pump pulses. The THz pulses have a peak field strength of 6.1 MV/cm and a center frequency of 20 THz; the probe pulses have photon energy of 1.4 ~ 2.4 eV. (b) Temporal profile of the applied THz bias transient. (c) Schematic picture of Wannier Stark localization. In the presence of strong external fields along the c axis, electronic states (orange: conduction band, blue: valence band) are localized to a few layers of ab plane, and energetically separated by $\Delta E_{WSL} = eE_{THz}c$ between adjacent lattice sites. Black arrows depict the interband transitions within the same site ($n = 0$) and between different sites ($n = \pm 1$). (d) The absorbance with and without the external transient biasing. The Wannier-Stark localization effectively reduces the 3D electronic structure into 2D layered structure along the ab plane, as depicted in blue together with the simplified 3D structure.

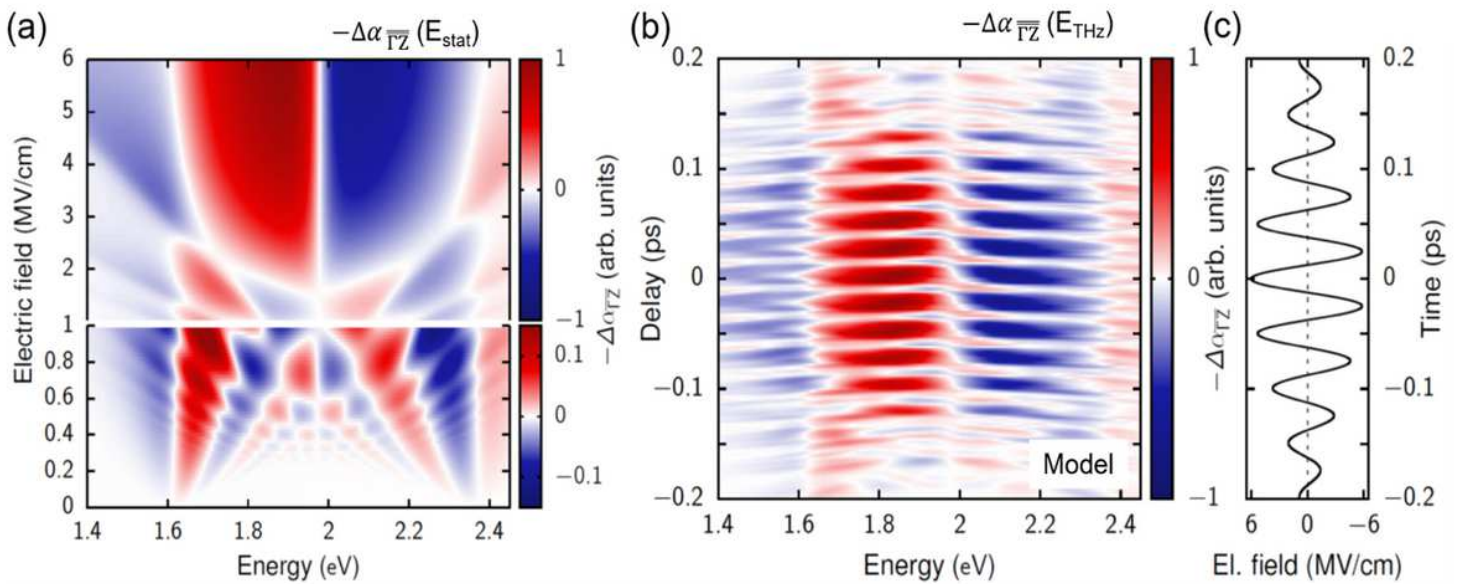


Figure 3

Numerical simulation of differential absorption spectra. Please see .pdf file for full caption

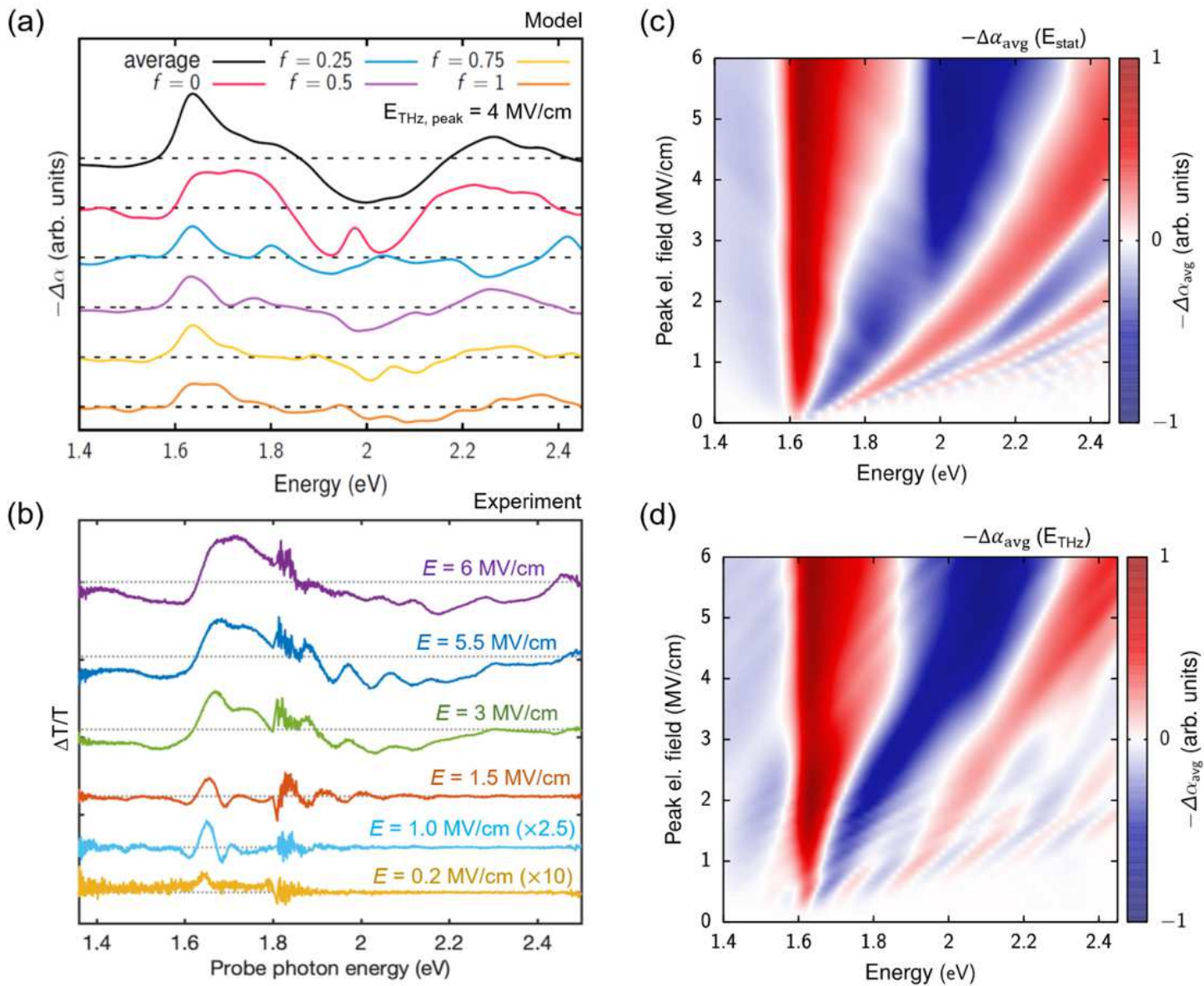


Figure 4

. Experiments on polycrystalline system and simulations with averaging of cosine band model from Γ to Γ direction. Please see .pdf file for full caption

Supplementary Files

This is a list of supplementary files associated with this preprint. Click to download.

- [SfinalNatComm.pdf](#)